

Universal and Experiment-calibrated Prediction of XANES through Crystal Graph Neural Network and Transfer Learning Strategy

Zichang Lin, Wenjie Chen, Yitao Lin, Xinxin Zhang, Yuegang Zhang
Department of Physics, Tsinghua University, Beijing 100084, China

Theoretical simulation is helpful for accurate interpretation of experimental X-ray absorption near-edge structure (XANES) spectra that contain rich atomic and electronic structure information of materials. However, current simulation methods are usually too complex to give the needed accuracy and timeliness when a large amount of data need to be analyzed, such as for in-situ characterization of battery materials. To address these problems, artificial intelligence (AI) models have been developed for XANES prediction. However, instead of using experimental XANES data, the existing models are trained using simulated data, resulting in significant discrepancies between the predicted and experimental spectra. Also, the universality across different elements has not been well studied for such models. In this work, we firstly establish a crystal graph neural network, pre-trained on simulated XANES data covering 48 elements, to achieve universal XANES prediction with a low average relative square error of 0.020223; and then utilize transfer learning to calibrate the model using a small experimental XANES dataset. After calibration, the edge energy misalignment error of the predicted S, Ti and Fe K edge XANES is significantly reduced by about 55%. The method demonstrated in this work opens up a new way to achieve fast, universal, and experiment-calibrated XANES prediction.

I. INTRODUCTION

X-ray absorption spectroscopy (XAS) is a powerful tool to detect the electronic structures and atomic geometry of materials, including atom valence, bond length and coordination number[1]. It has the advantages of non-destructive, element selectivity, and high sensitivity[2]. In addition, XAS is available for various sample types, such as bulk materials, powders, and solutions[3]. Therefore, it has been widely applied to study the problems in different areas, for example, low dimensional materials characterization[4, 5], catalytic mechanism analysis[6, 7], relics identification[8], and biomedical analyses[9]. Especially, these unique advantages enable XAS to combine with the operando/in-situ techniques for real-time characterization of some complex systems, like electrochemistry reactions in batteries[10–13]. According to the energy region with respect of the absorption edge, XAS can be divided into X-ray absorption near-edge structure (XANES) and extended X-ray absorption spectroscopy (EXAFS). EXAFS is mainly dominated by single scattering events, where coordination numbers and interatomic distances can be derived from Fourier transform for some materials with periodic structure[14, 15]. XANES is related to strong scattering processes as well as local atomic resonances, which is more complicated than EXAFS and hard to directly transformed to structure parameters[16]. Commonly, interpretation of experimental XANES is based on some empirical features, such as comparing edge shifts and peak positions with referenced spectra of standard materials[14].

With the development of XAS theory and the corresponding calculation software like FEFF9[17], FDMNES[18], and OCEAN[19], the XANES can be quantitatively simulated from a given crystal or molecule structure and taken as the referenced spectra in analysis. It helps to gain deeper insight into the relationship be-

tween local environment of absorbing atoms with spectra features. However, such calculation is time-consuming when the materials structure is complex. And the calculated spectra are sensitive to the selected approximation methods and calculation parameters, where a tedious parameters optimization process is needed to obtain reasonable results. In addition, XANES simulation faces challenges in aligning absolute energy scales and accounting for experimental broadening effects, resulting in inevitable discrepancies compared with experiments[20]. Without careful experimental calibration, the simulated XANES may yield false edge and peak features, misleading the XANES analysis. These shortcomings of current simulation methods have brought significant challenges for efficient and accurate XANES interpretation. This especially limits the in-situ XANES study of some essential but complex systems requiring massive data analysis, such as battery materials that experience constant structure changes during charge and discharge processes.

The development of artificial intelligent (AI) has opened up a new paradigm to solve the similar complex problems in different areas, such as AlphaFold for protein structure prediction[21], GNoME for material stable structures discovery[22], and DeepH for Hamiltonian calculation in DFT[23]. Researchers have also made some attempts to apply AI methods in XANES prediction to avoid the complex calculation process. These developed models cover the predictions on C K edge XANES of amorphous carbon and organic molecules[24, 25], O and N K edge XANES of molecules[26], and 3d transition metals K edge XANES of transition metal compounds[27–29]. Although those models offer a more efficient and convenient way to obtain XANES, their universality is challenged for they only focus on limited range of absorption elements. The universality of AI based XANES prediction on other common elements need to be further studied. In addition, due to the shortage

of experimental spectra, the existing models are trained based on the high throughput simulated XANES, where the spectra features and energy scale are not accurately calibrated. The uncorrected discrepancies between the training data and experiment measurement challenge the reliability of existing XANES prediction models. Therefore, the universality and fidelity of AI based XANES prediction should be improved before it can be put into practical use.

In this work, we explored the universal and experiment-calibrated prediction of XANES through crystal graph neural network and transfer learning strategy. A crystal graph neural network model for XANES prediction (CGXAS) is firstly established, and the universality of CGXAS on common detected elements of K edge XANES is studied. Then, transfer learning strategy is adopted to calibrate the predicted XANES using a small experimental dataset. The framework of CGXAS and the training flowchart is represented in Fig.1. In CGXAS, the graph neural network (GNN) encodes the local environment information into a latent site vector for each atom in the crystal graph. Then, the multilayer perceptron (MLP) decodes the site vector into the corresponded K edge XANES of each site. The successive mask pooling layer is used to average the XANES at each site according to the element, enabling XANES prediction for different elements in one network. A universal dataset with 341405 simulated XANES covering 48 elements[30] is used for CGXAS training and evaluation. This study compares three distinct approaches for achieving universal XANES prediction: (1) Training a single model (CGXAS_Uni) on the full dataset for universal XANES prediction; (2) Training individual element-specific CGXAS models using the element-specific subsets and assembling them for universal XANES prediction, where model for element X is denoted as CGXAS_Spec_X; (3) Fine-tuning CGXAS_Uni model on each element-specific subset, leading to CGXAS_FT_X model that represents the fine-tuned version for element X. Among the three models, the single CGXAS_Uni model demonstrated the best overall accuracy and universality. To study the interpretability of CGXAS, the t-SNE method is utilized to analyze the latent site vectors. Furthermore, to bridge the gap between simulation and experiment, transfer learning is also adopted to adapt the pretrained CGXAS_Uni model with a small experimental XANES dataset of element X, where the model after transfer learning is denoted as CGXAS_Exp_X. Compared with traditional learning process, transfer learning can transfer the knowledge learned in other domains to enhance the prediction performance on target domain[31]. Since the prediction performance of neural network is closely related with training data size, transferring simulated XANES knowledge to experimental XANES prediction can compensate the insufficiency in experimental data quantity. Here, we demonstrate the ability of transfer learning to calibrate the XANES prediction of S, Ti and

Fe K edge XANES using only 48, 40 and 45 experimental spectra for each element, where S, Ti, and Fe are the critical elements in the study of energy and catalysis. The calibrated CGXAS_Exp_S, CGXAS_Exp_Ti, and CGXAS_Exp_Fe models reduce the edge energy misalignment error of the predicted XANES by about 55%.

II. RESULTS

A. Universal XANES Prediction Performance of CGXAS

CGXAS_Uni is trained on the universal dataset which contains the K edge XANES spectra of elements in period 2 to 5 (noble gas elements are excluded). Fig.2a shows the evolution of training loss and validation loss, represented by the relative square error (RSE), in the 100 epochs. The definition of RSE is shown in Eq.1 at Methods section, where a RSE value closer to 0 stands for lower prediction loss. The training loss is reduced from 0.11 to 0.0093 after 100 epochs. And the validation loss converges to around 0.0207 after 70 epochs, which shows that 100 epochs are enough for model convergence. The distribution of test loss is shown in Fig.2(b), where most of the samples have the loss lower than 0.04. The average test loss is 0.020223, which is close to the validation loss. Examples of the predicted XANES spectra with low, medium, high, and ultra-high loss are shown in Fig.2(c)-(f), together with their simulated XANES spectra. It can be seen that CGXAS_Uni can predict the general spectrum features of edge energy and main peak reasonably well, and the prediction errors mainly come from the differences in peak intensity, peak width, and peak energy.

Besides training a single universal model, universal prediction of XANES can also be realized by assembling the element-specific models. The element-specific models can be either individually trained (CGXAS_Spec_X) or fine-tuned from CGXAS_Uni model (CGXAS_FT_X) on the element-specific subsets of universal dataset. To compare the performances of these distinct approaches for universal XANES prediction, the prediction accuracy of CGXAS_Uni, CGXAS_Spec_X, and CGXAS_FT_X on each absorption element is measured by the Pearson correlation coefficient (PCC) in testing set and shown in Fig.3(a). Here, a PCC value closer to 1 represents higher accuracy in prediction. For most of the elements, their CGXAS_Spec_X models can have high prediction accuracy (PCC>0.88). But for Be, Mg, Cd, Sb, and I, their CGXAS_Spec_X models have relative low accuracies (PCC<0.83). Compared with CGXAS_Spec_X models, CGXAS_Uni model yields enhanced prediction accuracies in almost all the elements. Especially for Be, Cd, Sb, and I, their PCCs are above 0.85 in CGXAS_Uni model; and O, S, Cl, and Se are the only 4 elements whose PCCs in CGXAS_Uni model are lower but with a negligible difference (<0.001) with those in CGXAS_Spec_X

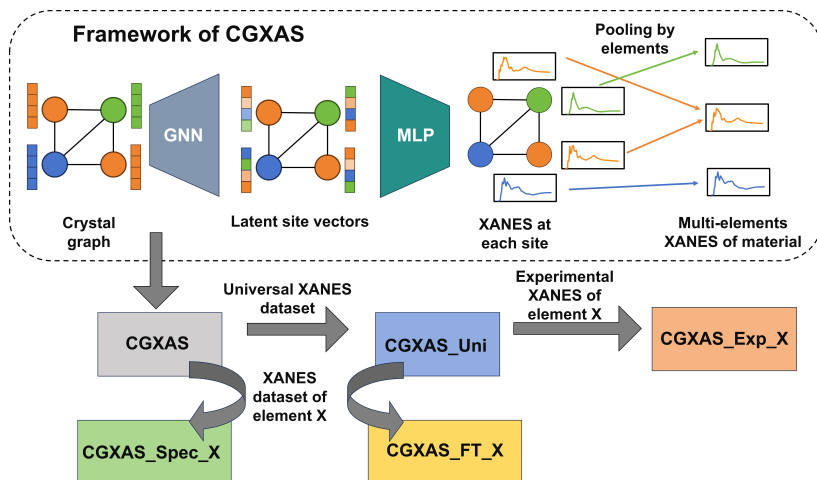


FIG. 1. Framework of CGXAS model and flowchart of training.

model. In general, therefore, the CGXAS_Uni model achieves better performance in universal XANES prediction than CGXAS_Spec_X models. The CGXAS_FT_X models have similar performances in all elements compared with CGXAS_Uni model. The average difference of PCC before and after fine-tuning is only around 0.002, showing that fine-tuning CGXAS_Uni on element-specific dataset has little influence on its accuracy. Comparing the XANES prediction performances of CGXAS_Uni, CGXAS_Spec_X and CGXAS_FT_X, it can be concluded that both accuracy and universality can be achieved by using the single CGXAS_Uni model. Therefore, the following interpretability and transfer learning study will only be conducted based on the CGXAS_Uni model.

B. Interpretability of CGXAS in XANES Prediction

XANES is determined by both the absorption atom and its local atomic environment[16]. To analyze the interpretability of CGXAS on XANES prediction, it is essential to verify whether the features of absorption atom and local atomic environment can be identified from the latent site vectors after the information gathering by graph neural network. Here, the t-distributed stochastic neighbor embedding (t-SNE) method[32] is applied to reduce the high dimension latent site vectors into 2 t-SNE features, so that they can be plotted in 2D space. Fig.3(b) shows the distribution of latent site vectors obtained from different absorption sites of various materials in the space of t-SNE features. Here, each element is marked by one specific color, which can be referred to by its atomic number in the color bar. In the figure, the points with the same color tend to form a cluster, and clusters of different colors are separated obviously. It means that the information of absorption element is still kept in the latent site vector, which can be extracted by the t-SNE method.

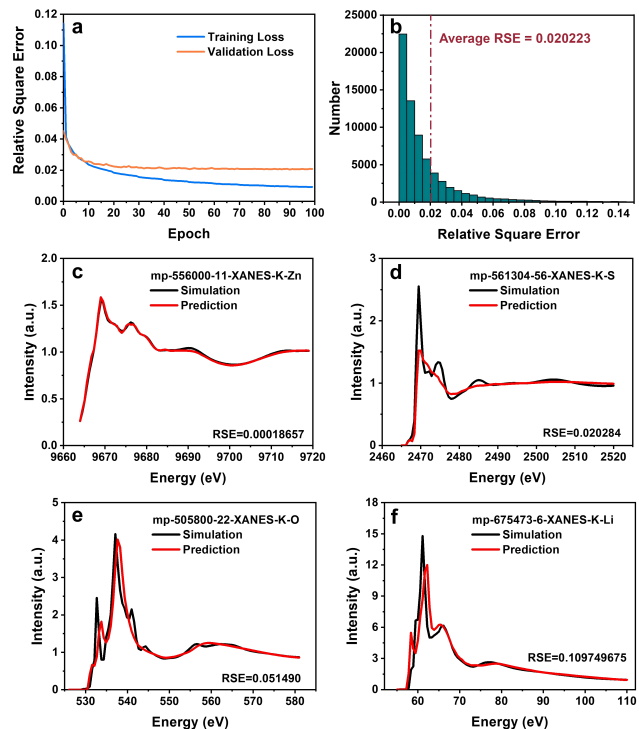


FIG. 2. Performance of CGXAS_Uni on the prediction of XANES. (a) Evolution of training loss and validation loss at each epoch in the training process, where the loss is measured by relative square error (RSE). (b) Distribution of prediction error in the testing set. (c)-(f) Examples of the predicted XANES with (c) low, (d) median, (e) high, and (f) ultra-high prediction error compared with simulated XANES.

The t-SNE features distribution of O latent site vectors obtained from oxides of different metal elements (Li, Mg, Al, Ti, Fe, and Cu) is shown in Fig.3(c), where the points of O sites are colored according to their neighboring elements. In the t-SNE feature space, these points

are grouped by the neighboring elements, and different groups are clearly separated. It indicates that the information of local atomic environment can also be extracted from the latent site vectors.

C. Transfer learning of CGXAS_Uni for Experiment-calibrated XANES Prediction

Since the CGXAS_Uni model is trained on simulated XANES dataset and there exists difference between the simulated and experimental data, it is not surprising that we also see difference between the predicted XANES and the experiments. Therefore, it is important to introduce experimental data to calibrate the model. However, the available experimental XANES data is very limited compared with that of the simulated XANES, making it hard to train a model with high accuracy using the experimental dataset alone. To address this problem, we explore the possibility of applying transfer learning to calibrate the CGXAS_Uni model with a small experimental dataset in this section. Here, three experimental datasets containing 48 S K edge XANES spectra, 40 Ti K edge XANES and 45 Fe K edge XANES are used in the transfer learning. The corresponded calibrated models are denoted as CGXAS_Exp_S, CGXAS_Exp_Ti, and CGXAS_Exp_Fe.

The samples distribution of these 3 experimental datasets is firstly analyzed and compared with the corresponded element specific simulated datasets respectively. To illustrate the sample distribution in the simulated dataset according to the spectrum features, their predicted spectra by CGXAS_Uni are transformed by t-SNE into two t-SNE features and plotted in the 2D space (blue dots in Fig.4). To evaluate the samples diversity of experimental datasets, the simulated spectra of the samples in experimental datasets predicted by CGXAS_Uni model are marked with red stars in the spectrum space. It can be seen that the samples from experimental datasets have a wide distribution among the samples from the large simulated dataset.

To assess the performance of transfer learning using a small experimental dataset, the dataset is randomly separated into training, validation and testing sets, with a fixed ratio of 6:1:1, for 20 times; and each separation is used to fine-tune and test an independent model. The average prediction losses in training, validation, and testing sets before and after transfer learning over the 20 models are shown in Fig.5(a), separately for CGXAS_Exp_S, CGXAS_Exp_Ti and CGXAS_Exp_Fe, where the error bar represents the standard deviation of loss. For CGXAS_Exp_S, the prediction losses before transfer learning are around 0.7, indicating that the simulated XANES has a large systematic error compared with the experiment measurement. The standard deviation of loss before transfer learning in the validation set (0.317) and testing set (0.305) are much larger than that in training set (0.0684), which is due to the smaller sample numbers in these two sets. After the

transfer learning, the average prediction losses are reduced by about 90% to around 0.07, showing the good performance of CGXAS_Exp_S. For CGXAS_Exp_Ti and CGXAS_Exp_Fe, the prediction losses before transfer learning are around 0.05 and 0.07 respectively. These losses are much smaller than that of CGXAS_S_Exp, because the peak intensity of Ti and Fe K edge XANES is not as high as S K edge XANES in general, making the misalignment of peak yield smaller value of RSE than S K edge XANES. After transfer learning, the prediction losses are still reduced to around 0.03 for both Ti and Fe K edge XANES, showing an accordant trend with CGXAS_Exp_S.

Energy misalignment in the simulated XANES will highly influence the accuracy of some key features like absorption edge energy. To assess the ability of transfer learning to calibrate the energy scale, the absolute errors of predicted edge energy are also analyzed and shown in Fig.5(b). Before transfer learning, the average errors of edge energy for the XANES of these three elements are around 4 eV. After the transfer learning, the average errors of edge energy are largely reduced by about 55%, from around 4 eV to around 1.8 eV. The results show that the transfer learning can effectively reduce the energy misalignment for different containing materials. Although an average error of 1.8 eV is still not enough for practical application, these results show the feasibility of the proposed method to calibrate the XANES prediction without a very huge experiment dataset.

To further illustrate the effect of transfer learning on experimental-calibrated XANES prediction, Fig.5(c)-(h) show the XANES spectra predicted by CGXAS_Exp_S, CGXAS_Exp_Ti and CGXAS_Exp_Fe with different RSE values, as well as the corresponded spectra predicted by CGXAS_Uni and experimental spectra. Before the transfer learning, most of the predicted XANES spectrum shows a similar shape as the experimental spectrum, but matches poorly in the absorption edge and peak positions. After the transfer learning even on a small experimental dataset, the absorption edge, the main peak positions and intensity are changed to achieve smaller difference with the experimental spectrum. For those examples with low RSE, the absorption edge and the main peak are corrected and fit well with the experimental spectrum. Some spectra have relatively high RSE but their edge and peak positions are still well corrected, where the high RSE mainly come from the large difference in main peak intensity. In general, for all the three cases of S, Ti, and Fe K edge XANES, the predicted XANES achieve better accordance with experimental results after transfer learning with a small experimental dataset, showing the good feasibility of our proposed method.

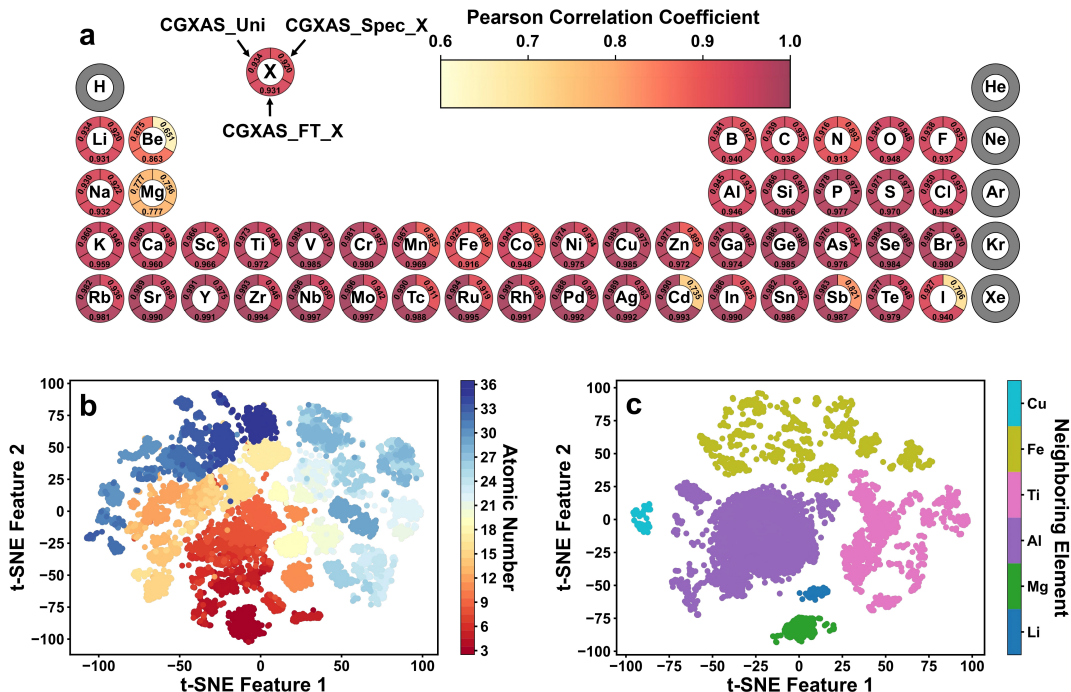


FIG. 3. Universality and interpretability analysis of CGXAS. (a) Comparison of XANES prediction accuracy (measured by Pearson correlation coefficient) of CGXAS_Uni, CGXAS.Spec_X, and CGXAS_FT_X in different elements. (b) Distribution of latent site vectors of different absorption sites, where the site vectors are reduced into 2 t-SNE features and colored according to their absorption elements. (c) Distribution of O latent site vectors obtained from Li, Mg, Al, Ti, Fe, and Cu metal oxides, where the site vectors are reduced into 2 t-SNE features and colored according to their neighboring elements. The latent site vectors in (b) and (c) are derived from CGXAS_Uni model.

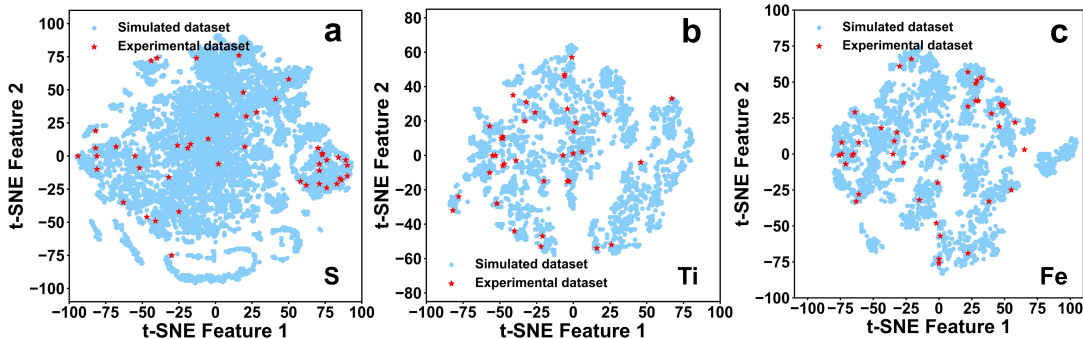


FIG. 4. Distribution of the samples from the simulated dataset and experimental dataset: (a) S K edge XANES, (b) Ti K edge XANES, (c) Fe K edge XANES. Here, the samples are represented by their spectra predicted by CGXAS_Uni and reduced into 2 features by t-SNE. The blue dot represents the samples from the simulated dataset, and the red star represents the samples from the experimental dataset.

III. DISCUSSION

Different ways to achieve universal XANES prediction are compared in this work. Directly training one CGXAS_Uni model on a universal XANES dataset shows better performance for XANES prediction of almost all the elements than training a CGXAS_Spec_X model on an element-specific XANES subset. Since the element-specific subset used in CGXAS_Spec_X comes completely

from the universal dataset for a specific element X, the enhanced XANES prediction performance of the CGXAS_Uni model must be attributed to other subsets of non-X elements in the universal dataset. Although the XANES spectra of different elements are significantly different regarding their energy ranges, the underlying physical rules for X-ray absorption and electron excitation are similar. Training model with the universal XANES dataset enables the neural network to learn the general underlying structure-XANES relationship regardless

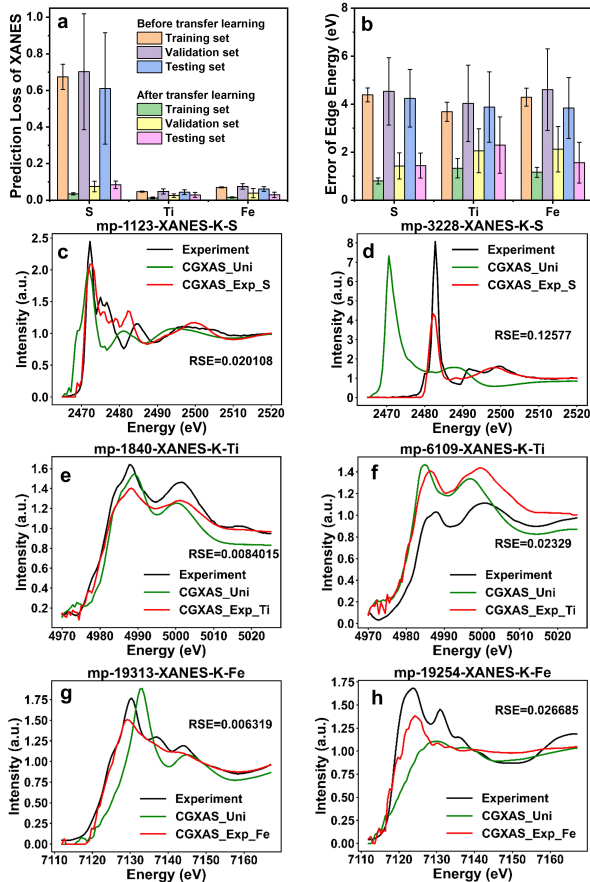


FIG. 5. Performance of the CGXAS model on the prediction of experimental XANES after transfer learning. (a) Prediction loss of S, Ti, and Fe K edge XANES (measured by RSE) before and after transfer learning in training set, validation set, and testing set. (b) Error of edge energy compared with experimental XANES before and after transfer learning in training set, validation set, and testing set. Here, the column height and error bar represent the average value and standard deviation of the prediction losses or energy errors calculated over 20 models trained with different data separations respectively. (a) and (b) share the same legend. (c)-(d) Examples of S K edge XANES predicted by CGXAS_Exp_S for the samples in testing sets with different RSE values, together with the spectrum predicted by CGXAS_Uni and the ground truth experimental XANES. (e)-(f) Examples of Ti K edge XANES predicted by CGXAS_Exp_Ti for the samples in testing sets. (g)-(h) Examples of Fe K edge XANES predicted by CGXAS_Exp_Fe for the samples in testing sets.

of the energy range for each element, thus enhancing the overall prediction accuracy for all elements. The fine-tuned CGXAS_FT_X model on the element-specific dataset has little influence on the prediction accuracy, implying that the knowledge of each element has already been well learned in the CGXAS_Uni model. In the previous work for 3d transition metal XANES prediction, Kharel et al. came out with an opposite result: the element specific model outperforms the universal model[27].

The cause the opposite results can be understood by the different structure features representations adopted in these two works. In this work, a GNN encoder is trained to process the structure information in the crystal graph, where a universal dataset containing more diverse structures is helpful to achieve better structure representations. In Kharel’s work, the universal dataset has no advantage in achieving better structure representations since a pretrained model is used for structure features encoding. On the contrary, the XANES prediction in universal model is more complex than that in element specific model, therefore yielding an opposite result. But pretraining on universal dataset can still reduce the overfitting risk for the finetuned universal model, therefore their finetuned universal models has better performance than the element specific models in general.

Through t-SNE analysis of the latent site vectors, the ability of CGXAS to extract the essential structural information related to XANES is verified, including absorption element, and neighboring atom type. The interpretability study and the excellent universality discussed earlier show that the XANES prediction of CGXAS_Uni is based on learning underlying physics rather than remembering the training data. The XANES prediction process of CGXAS can be qualitatively interpreted combining the XANES theory and the network architecture shown in Fig.1. In the initial crystal graph, each node only contains the information of the corresponding atom and is connected with its neighboring atoms by edges. During the processing of GNN, the information of neighboring atoms is gathered into the node through the edge connections. Therefore, the site vector on each node in the outputted graph contains the information of the scattering paths between the absorption atom and its local atomic environment. Then, MLP operates the latent site vector to predict the absorption coefficient at each energy grid.

By transfer learning on a small size experimental XANES dataset, the experimental-calibrated model can reduce the prediction loss and edge energy error compared with experimental XANES, respectively. The transfer learning strategy is helpful to break the dilemma between data fidelity and quantity. Pretrained on a large amount of low-fidelity simulated XANES enables CGXAS_Uni model to extract essential structure information from the given crystal graph. Then, the network parameters of MLP are adjusted using a small amount of high-fidelity experimental data in the transfer learning process, which can be defined as an experimental calibration of the prediction model. Although S, Ti and Fe elements are used as examples of our transfer learning, the pretrained CGXAS_Uni model can be easily extended to predict the experimental XANES of any other element with a similar transfer learning method.

It should be noted that the three experiment-calibrated models are developed for the purpose of proof-of-principles in this work. There some still some problems need to be solved before they can be put into practi-

cal use. For the peak width and some finer peaks in the high energy region, the experiment-calibrated models may give relatively large errors in the prediction. And there are also a few spectra with large discrepancy with experimental spectra. In future study, the universal, efficient, and experiment-based prediction of XANES can be further enhanced by obtaining more high-fidelity XANES data and developing more powerful AI algorithms, enabling the scientist to gain deeper insights into more complex scientific problems using XAS techniques.

IV. METHOD

A. Node and edge features representation

An atom in the crystal is represented by a node in the corresponding crystal graph. The atom features used in the CGXAS include the atomic number, period of atom, and the numbers of valence electrons in the s, p, d, and f orbitals, which are represented by their one-hot codes with the lengths of 101, 7, 3, 7, 11, 15 separately (shown in Fig.6(a)). These one-hot codes are concatenated as the node vector with the length of 146.

In the crystal graph, one atom is connected with the neighboring atoms within the cutoff radius of 8 Å through a directional edge. And the maximum number of neighbors per atom is 12 in this work. To keep the rotational invariance and encode the geometry information, the Gaussian basis set and the plane wave basis set are adopted as the edge features[33].

B. Model architecture of CGXAS

The model architecture of CGXAS is shown in Fig.6(b). The node features of the input graph are firstly embedded by an embedding layer. Then, the information of neighboring nodes is gathered to each node through the edge in the following graph convolution modules. Here, one graph convolution module is composed of a gated convolution layer of geo-CGNN[33], a normalization layer and a one layer perceptron. The updated node features of each graph convolution module ω^i are multiplied by $\frac{1}{i!}$ and summed over as the site vectors. The above modules together compose the GNN module in Fig.1. Next, the site vectors are processed by the multilayer perceptron and a Relu layer to generate the intensity of XANES of each absorption site. The activation function of the multilayer perceptron is Silu in this work. And the Relu layer is designed to avoid the prediction of negative intensity. Finally, the mask pooling layer will average the XANES over the unmasked sites, which is used to obtain the XANES of target site or specific element. The depths of gated convolution layers and multilayers perceptron are both five. The widths of input node features, hidden layer features and output spectrum are 146, 256 and 100 separately.

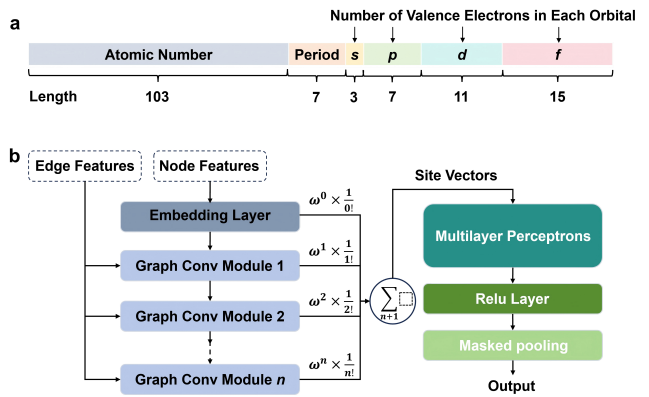


FIG. 6. Crystal graph representation and detailed architecture of CGXAS. (a) Node features of crystal graph. (b) Model architecture of CGXAS.

C. XANES dataset

The dataset of simulated K edge XANES spectra used in this work covers the elements from the second to fifth period except the rare gas elements. The crystal structures of materials are derived from the Materials Project[34, 35] using the pymatgen[36] and the XANES are obtained from an opensource XAS dataset generated through FEFF9[30]. Each XANES spectrum is matched with a distinct atom site in a material and is indexed by a unique id in the following format: “mp id - site index - spectrum type - edge type - absorption element”. For example, “mp-561304-56-XANES-K-S” represents the S K edge XANES of the 56th site of material “mp-561304” in Materials Project. For all the XANES spectra of the same element, a unified absorption energy range that can cover the pre-edge and near edge regions is chosen. And the XANES intensities at 100 uniform energy grid points in the corresponding element energy range are defined as the output of CGXAS. By fixing the absorption energy range of different elements, the multiple elements XANES can be predicted in the same neural network.

The experimental data used in transfer learning contains S K edge XANES of 48 different materials, Ti K edge XANES of 40 different materials, and Fe K edge XANES of 45 different materials. The spectra are obtained from beamline BL16U1 of the Shanghai Synchrotron Radiation Facility (SSRF), beamline 4B7A of Beijing Synchrotron Radiation Facility (BSRF), the XASLIB database (<https://xaslib.xrayabsorption.org/>), ESRF ID21 Sulfur XANES spectra database(<https://www.esrf.fr/home/UsersAndScience/Experiments/XNP/ID21/php.html>), MDR XAFS DB[37], and several literatures[38–57].

D. Training of CGXAS with simulated XANES

The simulated XANES dataset is divided into training set, validation set and testing set by the ratio of 6:2:2. The relative square error (RSE) between the actual spectrum μ_i^a and predicted spectrum μ_i^p is used as the loss metric in the training process of CGXAS_Uni and CGXAS_Spec_X:

$$\text{RSE} = \frac{\sum_{i=1}^{100} (\mu_i^a - \mu_i^p)^2}{\sum_{i=1}^{100} (\mu_i^a)^2}, \quad (1)$$

Adam optimizer and an initial learning rate of 0.0001 are chosen to optimize the parameters of neural network. The maximum number of epochs of training is 100. In the fine-tuning process of CGXAS_FT_X, only the parameters in the MLP are optimized while other layers in the network are unchanged. The loss metric and the hyperparameters of fine-tuning of CGXAS_FT_X are the same as the training process of CGXAS_Uni and CGXAS_Spec_X. Pearson correlation coefficient (PCC) is also used to analyze the prediction accuracy of XANES in the work. The PCC between μ_i^a and μ_i^p is defined as:

$$\text{PCC} = \frac{\sum_{i=1}^{100} (\mu_i^a - \bar{\mu}_i^a)^2 (\mu_i^p - \bar{\mu}_i^p)^2}{\sqrt{\sum_{i=1}^{100} (\mu_i^a - \bar{\mu}_i^a)^2} \sqrt{\sum_{i=1}^{100} (\mu_i^p - \bar{\mu}_i^p)^2}}, \quad (2)$$

where $\bar{\mu}_i^a = \frac{1}{100} \sum_{i=1}^{100} \mu_i^a$ and $\bar{\mu}_i^p = \frac{1}{100} \sum_{i=1}^{100} \mu_i^p$. A PCC value closer to 1 means that the predicted spectrum has higher accuracy.

E. Transfer learning using experimental XANES

In the transfer learning of CGXAS_Exp_X, the pre-trained CGXAS_Uni on massive simulated XANES is fine-tuned on the experimental XANES. To avoid over fitting, only the parameters of MLP are optimized layer by layer while the other parts of network remain the same as the pretrained model. The loss metric used in transfer learning is RSE. And the size of training, validation and testing set have a ratio of 6:1:1. The Adam optimizer and an initial learning rate of 0.0001 are chosen to optimize the layer of MLP. The maximum number of training epochs of each layer is 30.

V. ACKNOWLEDGMENTS

This work was supported by the National Key R&D Program of China (2022YFA1203400) and the National Natural Science Foundation of China (W2441009). The authors thank the 4B7A Beamline of Beijing Synchrotron Radiation Facility (<https://cstr.cn/31109.02.BSRF.4B7A>), BL16U Beamline of Shanghai Synchrotron Radiation Facility (<https://cstr.cn/31124.02.SSRF.BL16U1>) and Experiment Assist System of Shanghai Synchrotron Radiation Facility (<https://cstr.cn/31124.02.SSRF.LAB>) for providing technical support and assistance in XANES data collection.

-
- [1] D. Ketenoglu, *X-Ray Spectrometry* **51**, 422 (2022).
- [2] B. V. Kerr, H. J. King, C. F. Garibello, P. R. Dissanayake, A. N. Simonov, B. Johannessen, D. S. Eldridge, and R. K. Hocking, *Energy & Fuels* **36**, 2369 (2022).
- [3] C. T. Chantler, G. Bunker, P. D'Angelo, and S. Diaz-Moreno, *Nature Reviews Methods Primers* **4**, 89 (2024).
- [4] J. J. Velasco-Velez, C. H. Wu, B. Y. Wang, Y. Sun, Y. Zhang, J. H. Guo, and M. Salmeron, *The Journal of Physical Chemistry C* **118**, 25456 (2014).
- [5] J. J. Velasco-Velez, C.-H. Chuang, H.-L. Han, I. Martin-Fernandez, C. Martinez, W.-F. Pong, Y.-R. Shen, F. Wang, Y. Zhang, J. Guo, and M. Salmeron, *Journal of The Electrochemical Society* **160**, C445 (2013).
- [6] M. Cai, S. Sun, and J. Bao, *ChemPhysChem* **25**, e202300939 (2024).
- [7] B. Wu, T. Sun, Y. You, H. Meng, D. M. Morales, M. Lounasvuori, A. Beheshti Askari, L. Jiang, F. Zeng, B. Hu, X. Zhang, R. Tai, Z. J. Xu, T. Petit, and L. Mai, *Angewandte Chemie International Edition* **62**, e202219188 (2023).
- [8] M. Abúfn, A. Serrano, J. Chaboy, M. A. García, and N. Carmona, *Journal of Analytical Atomic Spectrometry* **28**, 1118 (2013).
- [9] F. Porcaro, S. Roudeau, A. Carmona, and R. Ortega, *TrAC Trends in Analytical Chemistry* **104**, 22 (2018).
- [10] Y. Xu, Y. Ye, S. Zhao, J. Feng, J. Li, H. Chen, A. Yang, F. Shi, L. Jia, Y. Wu, X. Yu, P.-A. Glans-Suzuki, Y. Cui, J. Guo, and Y. Zhang, *Nano Letters* **19**, 2928 (2019).
- [11] L. Jia, J. Wang, S. Ren, G. Ren, X. Jin, L. Kao, X. Feng, F. Yang, Q. Wang, L. Pan, Q. Li, Y.-s. Liu, Y. Wu, G. Liu, J. Feng, S. Fan, Y. Ye, J. Guo, and Y. Zhang, *ENERGY & ENVIRONMENTAL MATERIALS* **4**, 222 (2021).
- [12] S. Rehman, M. Pope, S. Tao, and E. McCalla, *Energy & Environmental Science* **15**, 1423 (2022).
- [13] S. Chen, C. Ma, Z. Li, and J. Zhou, *Carbon Neutralization* **4**, e70003 (2025).
- [14] A. A. Guda, S. A. Guda, K. A. Lomachenko, M. A. Soldatov, I. A. Pankin, A. V. Soldatov, L. Braglia, A. L. Bugaev, A. Martini, M. Signorile, E. Groppo, A. Piovano, E. Borfecchia, and C. Lamberti, *Catalysis Today* **336**, 3 (2019).
- [15] J. Timoshenko, F. T. Haase, S. Saddeler, M. Rüscher, H. S. Jeon, A. Herzog, U. Hejral, A. Bergmann, S. Schulz, and B. Roldan Cuenya, *Journal of the American Chemical Society* **145**, 4065 (2023).
- [16] J. J. Rehr and R. C. Albers, *Reviews of Modern Physics* **72**, 621 (2000).
- [17] J. J. Rehr, J. J. Kas, M. P. Prange, A. P. Sorini, Y. Takimoto, and F. Vila, *Comptes Rendus Physique* **10**, 548

- (2009).
- [18] O. Bunău and Y. Joly, *Journal of Physics: Condensed Matter* **21**, 345501 (2009).
- [19] J. Vinson, *Physical Chemistry Chemical Physics* **24**, 12787 (2022).
- [20] F. Meng, B. Maurer, F. Peschel, S. Selcuk, M. Hybertsen, X. Qu, C. Vorwerk, C. Draxl, J. Vinson, and D. Lu, *Physical Review Materials* **8**, 013801 (2024).
- [21] J. Jumper, R. Evans, A. Pritzel, T. Green, M. Figurnov, O. Ronneberger, K. Tunyasuvunakool, R. Bates, A. Židek, A. Potapenko, A. Bridgland, C. Meyer, S. A. A. Kohl, A. J. Ballard, A. Cowie, B. Romera-Paredes, S. Nikolov, R. Jain, J. Adler, T. Back, S. Petersen, D. Reiman, E. Clancy, M. Zielinski, M. Steinegger, M. Pacholska, T. Berghammer, S. Bodenstein, D. Silver, O. Vinyals, A. W. Senior, K. Kavukcuoglu, P. Kohli, and D. Hassabis, *Nature* **596**, 583 (2021).
- [22] A. Merchant, S. Batzner, S. S. Schoenholz, M. Aykol, G. Cheon, and E. D. Cubuk, *Nature* **624**, 80 (2023).
- [23] Y. Wang, Y. Li, Z. Tang, H. Li, Z. Yuan, H. Tao, N. Zou, T. Bao, X. Liang, Z. Chen, S. Xu, C. Bian, Z. Xu, C. Wang, C. Si, W. Duan, and Y. Xu, *Science Bulletin* **69**, 2514 (2024).
- [24] A. Kotobi, K. Singh, D. Höche, S. Bari, R. H. Meißner, and A. Bande, *Journal of the American Chemical Society* **145**, 22584 (2023).
- [25] H. Kwon, W. Sun, T. Hsu, W. Jeong, F. Aydin, S. Sharma, F. Meng, M. R. Carbone, X. Chen, D. Lu, L. F. Wan, M. H. Nielsen, and T. A. Pham, *The Journal of Physical Chemistry C* **127**, 16473 (2023).
- [26] M. R. Carbone, M. Topsakal, D. Lu, and S. Yoo, *Physical Review Letters* **124**, 156401 (2020).
- [27] S. R. Kharel, F. Meng, X. Qu, M. R. Carbone, and D. Lu, *Physical Review Materials* **9**, 043803 (2025).
- [28] C. D. Rankine, M. M. M. Madkhali, and T. J. Penfold, *The Journal of Physical Chemistry A* **124**, 4263 (2020).
- [29] C. D. Rankine and T. J. Penfold, *The Journal of Chemical Physics* **156**, 164102 (2022).
- [30] K. Mathew, C. Zheng, D. Winston, C. Chen, A. Dozier, J. J. Rehr, S. P. Ong, and K. A. Persson, *Scientific Data* **5**, 180151 (2018).
- [31] S. J. Pan and Q. Yang, *IEEE Transactions on Knowledge and Data Engineering* **22**, 1345 (2010).
- [32] L. van der Maaten and G. Hinton, *Journal of Machine Learning Research* **9**, 2579 (2008).
- [33] J. Cheng, C. Zhang, and L. Dong, *Communications Materials* **2**, 92 (2021).
- [34] M. K. Horton, P. Huck, R. X. Yang, J. M. Munro, S. Dwaraknath, A. M. Ganose, R. S. Kingsbury, M. Wen, J. X. Shen, T. S. Mathis, A. D. Kaplan, K. Berket, J. Riebesell, J. George, A. S. Rosen, E. W. C. Spotte-Smith, M. J. McDermott, O. A. Cohen, A. Dunn, M. C. Kuner, G.-M. Rignanese, G. Petretto, D. Waroquiers, S. M. Griffin, J. B. Neaton, D. C. Chrzan, M. Asta, G. Hautier, S. Cholia, G. Ceder, S. P. Ong, A. Jain, and K. A. Persson, *Nature Materials* **24**, 1522 (2025).
- [35] A. Jain, S. P. Ong, G. Hautier, W. Chen, W. D. Richards, S. Dacek, S. Cholia, D. Gunter, D. Skinner, G. Ceder, and K. A. Persson, *APL Materials* **1**, 011002 (2013).
- [36] S. P. Ong, W. D. Richards, A. Jain, G. Hautier, M. Kocher, S. Cholia, D. Gunter, V. L. Chevrier, K. A. Persson, and G. Ceder, *Computational Materials Science* **68**, 314 (2013).
- [37] M. Ishii, K. Tanabe, A. Matsuda, H. Ofuchi, T. Matsumoto, T. Yaji, Y. Inada, H. Nitani, M. Kimura, and K. Asakura, *Science and Technology of Advanced Materials: Methods* **3**, 2197518 (2023).
- [38] H. Guo, M. R. Carbone, C. Cao, J. Qu, Y. Du, S.-M. Bak, C. Weiland, F. Wang, S. Yoo, N. Artrith, A. Urban, and D. Lu, *Scientific Data* **10**, 349 (2023).
- [39] S. A. Azzam, A. Boubnov, A. S. Hoffman, T. López-Ausens, N. Chiang, G. Canning, P. Sautet, S. R. Bare, and D. A. Simonetti, *Inorganic Chemistry* **59**, 15276 (2020).
- [40] J. T. Kim, A. Rao, H.-Y. Nie, Y. Hu, W. Li, F. Zhao, S. Deng, X. Hao, J. Fu, J. Luo, H. Duan, C. Wang, C. V. Singh, and X. Sun, *Nature Communications* **14**, 6404 (2023).
- [41] D.-Y. Cho, L. Xi, C. Boothroyd, B. Kardynal, and Y. M. Lam, *Scientific Reports* **6**, 22818 (2016).
- [42] A.-K. Yadav, W. Ma, P. Abi Younes, G. Ciatto, N. Gauthier, E. Skopin, E. A. Quadrelli, N. Schneider, and H. Renevier, *Nanoscale* **16**, 1853 (2024).
- [43] D. Li, G. M. Bancroft, M. Kasrai, M. E. Fleet, B. X. Yang, X. H. Feng, K. Tan, and M. Peng, *Physics and Chemistry of Minerals* **20**, 489 (1994).
- [44] M. E. Fleet, S. L. Harmer, X. Liu, and H. W. Nesbitt, *Surface Science* **584**, 133 (2005).
- [45] Y. Gorlin, A. Siebel, M. Piana, T. Huthwelker, H. Jha, G. Monsch, F. Kraus, H. A. Gasteiger, and M. Tromp, *Journal of The Electrochemical Society* **162**, A1146 (2015).
- [46] S. P. Farrell, M. E. Fleet, I. E. Stekhin, A. Kravtsova, A. V. Soldatov, and X. Liu, *American Mineralogist* **87**, 1321 (2002).
- [47] M. E. Fleet, X. Liu, S. L. Harmer, and H. W. Nesbitt, *The Canadian Mineralogist* **43**, 1589 (2005).
- [48] A. V. Soldatov, A. N. Kravtsova, M. E. Fleet, and S. L. Harmer, *Journal of Physics: Condensed Matter* **16**, 7545 (2004).
- [49] W. Klysubun, P. Tarawarakarn, P. Sombunchoo, S. Klinkhieo, J. Chaiprapa, and P. Songsiriritthigul, *AIP Conference Proceedings* **879**, 860 (2007).
- [50] E. R. Aluri and A. P. Grosvenor, *Journal of Physics and Chemistry of Solids* **74**, 830 (2013).
- [51] M. Wilke, F. Farges, P.-E. Petit, J. Brown, Gordon E., and F. Martin, *American Mineralogist* **86**, 714 (2001).
- [52] P. E. R. Blanchard, S. Liu, B. J. Kennedy, C. D. Ling, Z. Zhang, M. Avdeev, L.-Y. Jang, J.-F. Lee, C.-W. Pao, and J.-L. Chen, *Dalton Transactions* **43**, 17358 (2014).
- [53] F. Farges, G. E. Brown, and J. J. Rehr, *Physical Review B* **56**, 1809 (1997).
- [54] C. Lawley, M. Nachttegaal, J. Stahn, V. Roddatis, M. Döbeli, T. J. Schmidt, D. Pergolesi, and T. Lippert, *Nature Communications* **11**, 1728 (2020).
- [55] F. P. Leitzke, R. O. C. Fonseca, J. Göttlicher, R. Steininger, S. Jahn, C. Prescher, and M. Lagos, *Contributions to Mineralogy and Petrology* **173**, 103 (2018).
- [56] P. Y. Raval, N. P. Joshi, P. R. Pansara, N. H. Vasoya, S. Kumar, S. N. Dolia, K. B. Modi, and R. K. Singhal, *Ceramics International* **44**, 20716 (2018).
- [57] S. Zhou, Y. Zhao, R. Shi, Y. Wang, A. Ashok, F. Héraly, T. Zhang, and J. Yuan, *Advanced Materials* **34**, 2204388 (2022).